

1 **A “bottle-around-ship” like method synthesized yolk-shell Ag<sub>3</sub>PO<sub>4</sub>@MIL-53(Fe)**

2 **Z-scheme photocatalysts for enhanced tetracycline removal**

3 Xiaopei Li<sup>a,1</sup>, Zhuotong Zeng<sup>b,1</sup>, Guangming Zeng<sup>a,\*</sup>, Dongbo Wang<sup>a,\*</sup>, Rong Xiao<sup>b,\*</sup>, Yingrong Wang<sup>a</sup>, Chenyun  
4 Zhou<sup>a</sup>, Huan Yi<sup>a</sup>, Shujing Ye<sup>a</sup>, Yang Yang<sup>a</sup>, Weiping Xiong<sup>a</sup>

5 <sup>a</sup>College of Environmental Science and Engineering, Hunan University and Laboratory of Environmental  
6 Biology and Pollution Control (Hunan University), Ministry of Education, Changsha 410082, P.R.China;

7 <sup>b</sup> Department of Dermatology, Second Xiangya Hospital, Central South University, Changsha 410011, P R  
8 China.

9  
10 \*Corresponding author. Tel.: +86 731 88823701; Fax: +86 731 88823701

11 E-mail addresses: [zgming@hnu.edu.cn](mailto:zgming@hnu.edu.cn) (G. Zeng), [dongbowang@hnu.edu.cn](mailto:dongbowang@hnu.edu.cn) (D. Wang) and  
12 [xiaorong65@csu.edu.cn](mailto:xiaorong65@csu.edu.cn) (R. Xiao).

13 <sup>1</sup> These authors contribute equally to this article.

Accepted MS

14 **Abstract:**

15 A novel yolk-shell  $\text{Ag}_3\text{PO}_4@\text{MIL-53}(\text{Fe})$  Z-scheme photocatalyst was fabricated via a “bottle-around-ship” like  
16 method. Experiments on the treatment of tetracycline upon visible light irradiation showed that the as-prepared  
17 photocatalyst possessed excellent photocatalytic performance. Experimental results showed that tetracycline  
18 removal efficiency of the yolk-shell  $\text{Ag}_3\text{PO}_4@\text{MIL-53}(\text{Fe})$  Z-scheme photocatalyst was almost 3 times higher  
19 than that of MIL-53(Fe). The enhanced photocatalytic performance of  $\text{Ag}_3\text{PO}_4@\text{MIL-53}(\text{Fe})$  nanocomposite  
20 could be contributed to its higher surface area, better absorption capability, and greater charge separation  
21 efficiency. In addition, the  $\text{H}_2\text{O}_2$  concentration detection results for  $\text{Ag}_3\text{PO}_4$  (54  $\mu\text{mol/L}$ ) and  $\text{Ag}_3\text{PO}_4@\text{MIL-}$   
22 53(Fe) (52  $\mu\text{mol/L}$ ) indicated that a big part of generated  $\text{H}_2\text{O}_2$  on the  $\text{Ag}_3\text{PO}_4$  core would be quickly  
23 decomposed by the MIL-53(Fe) shell and generated more reactive species through the photo-Fenton-like  
24 reaction, which is beneficial for the improvement of photocatalytic performance. This is a promising approach  
25 to fabricate yolk-shell structure photocatalyst and a different aspect to design multiple semiconductor  
26 composites heterojunction for environmental remediation.

27 **Keywords:**  $\text{Ag}_3\text{PO}_4$ , MIL-53(Fe), yolk-shell structure, Z-scheme photocatalyst, tetracycline

28 **1. Introduction**

29 With the development of the time, the use of antibiotics has increased sharply, which not only damages the  
30 ecosystem, but also poses a threat to human health. It is urgent to remove antibiotic pollutants from the  
31 environment [1-10]. For instance, tetracycline (TC), one of extensively used antibiotics, which is hardly to be  
32 metabolized by human beings or animals, and could accumulate in the natural environment at significant levels.  
33 For example, the maximum concentration of TC in Yangtze River, China was 312 ng/g, while the minimum  
34 detection concentration of TC was 100 ng/g [11]. Owing to its chemical stability and antibacterial nature, it is  
35 difficult to be removed by traditional wastewater treatment. Thus, effective removal of TC in the environment

36 is imperative [12]. Various methods were tested to solve this problem in the past, such as membrane filtration  
37 [13], adsorption [14], Fenton-reaction[15], and photocatalysis [16-20]. Among them, photocatalysis has gained  
38 significant attention on account of its low cost, low toxicity, and superb degradation efficiency [21-24].

39 Metal-organic frameworks (MOFs) was constituted by straightforward self-assembly of metal ions or  
40 clusters with organic linkers [25, 26]. MOF materials offer an ideal platform for rationally combined light-  
41 harvesting components and catalytic activity centers in one system and shows better performance [27]. Hence,  
42 MOF materials could be considered as photocatalysts with unlimited potential. Among numerous MOF  
43 materials, MIL-53(Fe) has gained extensive interests in the fields of hydrogen generation, catalysis, drug  
44 delivery, and gas storage [28-31]. The Fe-O clusters could be activated upon visible light irradiation, which  
45 makes MIL-53(Fe) available for visible light photocatalysis. However, owing to its high recombination rate of  
46 photoinduced carriers, MIL-53(Fe) shows unsatisfied photocatalytic performance.

47 To solve this problem, constructing a Z-scheme heterostructure seems to be a feasible way. Among various  
48 Ag-based materials,  $\text{Ag}_3\text{PO}_4$  is a type of photocatalyst which possesses superior photo-oxidation capability [32-  
49 35]. However, owing to the limit by its conduction band position (0.45 eV vs. normal hydrogen electrode (NHE),  
50 pH=0), the photogenerated electrons of  $\text{Ag}_3\text{PO}_4$  could be absorbed by  $\text{Ag}^+$  released from the lattice of  $\text{Ag}_3\text{PO}_4$   
51 ( $4\text{Ag}_3\text{PO}_4 + 6\text{H}_2\text{O} + 12\text{h}^+ + 12\text{e}^- \rightarrow 2\text{Ag} + 4\text{H}_3\text{PO}_4 + 3\text{O}_2$ ), instead of  $\text{H}_2\text{O}$  if there were no scavengers being  
52 existed. In addition, it is uneconomical that using pure  $\text{Ag}_3\text{PO}_4$  for the degradation of pollutants or splitting  
53 water for  $\text{O}_2$  due to the existence of noble material silver.

54 Previous publications demonstrated that nanoparticles could be surrounded by MOFs via “bottle-around-  
55 ship” approach [36]. In addition, plenty of  $\text{Ag}_3\text{PO}_4$ @MOF composites was proven to be efficient photocatalysts  
56 for various applications [37-43]. This enlightened us to introduce a small amount of  $\text{Ag}_3\text{PO}_4$  into MIL-53(Fe)  
57 through “bottle-around-ship” like method to construct a yolk-shell Z-scheme photocatalyst and to consume the

58 photogenerated electrons of  $\text{Ag}_3\text{PO}_4$  with the holes generated by MIL-53(Fe), for the boost of photocatalytic  
59 activity and restrain the photocorrosion of  $\text{Ag}_3\text{PO}_4$ . Besides, it was reported that there would be little amount of  
60  $\text{H}_2\text{O}_2$  generated during the photoreaction process of  $\text{Ag}_3\text{PO}_4$  ( $\text{O}_2 + 2\text{H}^+ + 2\text{e}^- \rightarrow \text{H}_2\text{O}_2$  (0.68V vs NHE)), which  
61 would consume the photogenerated holes of  $\text{Ag}_3\text{PO}_4$  ( $\text{H}_2\text{O}_2 + 2\text{h}^+(\text{Ag}_3\text{PO}_4) \rightarrow \text{O}_2 + 2\text{H}^+$ ), and are adverse to the  
62 photocatalytic activity [44, 45]. Accordingly, the photogenerated  $\text{H}_2\text{O}_2$  from  $\text{Ag}_3\text{PO}_4$  could be utilized by  
63 materials with  $\text{Fe}^{3+}$  through Fenton reaction [46]. Hence, it is assumed that combining  $\text{Ag}_3\text{PO}_4$  with MIL-53(Fe)  
64 could take advantage of this  $\text{H}_2\text{O}_2$  through a photo-Fenton-like reaction, further improved the photocatalytic  
65 performance of this composite. There is no such article available on the preparation of yolk-shell  $\text{Ag}_3\text{PO}_4$ @MIL-  
66 53(Fe) hybrid photocatalyst for the adsorption and removal of TC.

67 The present work aims to examine the feasibility of yolk-shell  $\text{Ag}_3\text{PO}_4$ @MIL-53(Fe) hybrids for enhancing  
68 TC removal. Firstly, the effect of  $\text{Ag}_3\text{PO}_4$  dosage on TC removal was investigated under different TC  
69 concentrations. Quenching experiments and electron spin resonance (ESR) tests were then used to identify the  
70 dominant reactive species in this system. Besides, the concentration determination of  $\text{H}_2\text{O}_2$  in the photoreaction  
71 was further tested. Photocatalytic stability of  $\text{Ag}_3\text{PO}_4$  and  $\text{Ag}_3\text{PO}_4$ @MIL-53(Fe) was evaluated after five cycles.  
72 At last, we proposed the possible mechanism of  $\text{Ag}_3\text{PO}_4$ @MIL-53(Fe) hybrids in detail.

## 73 2. Experimental

74 This section was depicted in the Supplementary information (SI).

## 75 3. Results and discussions

76 By controlling the amount of  $\text{Ag}_3\text{PO}_4$ ,  $\text{Ag}_3\text{PO}_4$ @MIL-53(Fe) composites with different mass ratio (MIL-  
77 53(Fe) :  $\text{Ag}_3\text{PO}_4$  = 5 : 1, 10 : 1, 20 : 1, 50 : 1, 100 : 1) were denoted as M:A=5:1, M:A=10:1, M:A=20:1,  
78 M:A=50:1, and M:A=100:1. In this section, M:A=5:1, M:A=10:1, M:A=20:1, MIL-53(Fe) samples were  
79 characterized by X-ray diffraction (XRD) to investigate their crystallographic structure. As depicted in fig 1A,

80 the diffraction peaks of bare MIL-53(Fe) (marked with ★) were sharp and clear, indicating it possesses high  
81 crystallinity. All the diffraction peaks of bare MIL-53(Fe) sample were in agreement with the previous reports  
82 [47, 48]. Four distinct diffraction peaks of  $\text{Ag}_3\text{PO}_4$  (marked with ☆) at  $33.3^\circ$ ,  $47.8^\circ$ ,  $55.0^\circ$ , and  $57.3^\circ$  could be  
83 detected in the  $\text{Ag}_3\text{PO}_4@\text{MIL-53(Fe)}$  samples, which were related to the (210), (310), (320) and (321) planes  
84 of  $\text{Ag}_3\text{PO}_4$  [49]. All modified samples displayed the characteristic peaks of  $\text{Ag}_3\text{PO}_4$  and MIL-53(Fe), and no  
85 peaks related to other material were detected, suggesting the successful formation of  $\text{Ag}_3\text{PO}_4@\text{MIL-53(Fe)}$   
86 samples. When the proportion of  $\text{Ag}_3\text{PO}_4$  increased, the diffraction peaks intensities at  $2\theta = 12.5^\circ$  and  $18.5^\circ$  of  
87 MIL-53(Fe) decreased, which indicated that the bring in of  $\text{Ag}_3\text{PO}_4$  particles in the MIL-53(Fe) synthesis  
88 procedure may restrain some planes of MIL-53(Fe) growth. Moreover, no observation of characteristic peak  
89 position of MIL-53(Fe) shifting in the  $\text{Ag}_3\text{PO}_4@\text{MIL-53(Fe)}$  sample, suggesting that the crystal structure was  
90 not destroyed by the introduction of  $\text{Ag}_3\text{PO}_4$  in the synthesis process.

91 The detailed molecular structure and functional groups information were characterized by Fourier  
92 transformed infrared spectra (FT-IR). As illustrated in Fig 1B, the absorption peaks located at 1690, 1567, 1386,  
93 750, and  $545\text{ cm}^{-1}$  could be detected in the spectrum of MIL-53(Fe) sample. The absorption peak at  $1690\text{ cm}^{-1}$   
94 was corresponded to C=O stretching mode [50]. Peaks at 1567 and  $1386\text{ cm}^{-1}$  were assigned to symmetric and  
95 asymmetric vibrations of carboxyl groups, respectively [51]. The peak at  $750\text{ cm}^{-1}$  results from the C—H  
96 bonding vibrations in the benzene rings, while the peak at  $545\text{ cm}^{-1}$  could be ascribed to the stretching vibration  
97 of F—O bond [52-54]. For bare  $\text{Ag}_3\text{PO}_4$ , two peaks located at 1072 and  $550\text{ cm}^{-1}$  were presented, which could  
98 be allocated to the P—O stretching vibration of  $\text{PO}_4^{3-}$  and O=P—O flexural vibrations, respectively [55]. For  
99 M:A=10:1 sample, the peak located at  $1386\text{ cm}^{-1}$  was not observed, indicating that the symmetric vibrations of  
100 carboxyl groups may be destroyed by the introduction of  $\text{Ag}_3\text{PO}_4$  during the synthesis process. Other  
101 characteristic peaks of MIL-53(Fe) and  $\text{Ag}_3\text{PO}_4$  were clearly displayed in the spectrum of M:A=10:1 sample,

102 indicating the successful synthesis of Ag<sub>3</sub>PO<sub>4</sub>@MIL-53(Fe) composite.

103 X-ray photoelectron spectra (XPS) technique was used to characterize M:A=10:1 sample to further obtain  
104 information about chemical states and surface composition. As depicted in the survey spectra (fig 2A), peaks  
105 corresponding to Fe, O, Ag, C, and P elements were presented, which was in agreement with the composite of  
106 M:A=10:1. In the C 1s XPS spectrum (fig 2B), the peak located at 284.8 eV was belonging to the benzoic rings,  
107 and the peak at 288.6 eV could be assigned to the carboxylate groups of H<sub>2</sub>BDC [56]. In the Fe 2p (fig 2C)  
108 spectrum, two peaks centered at 712.3 eV and 726.0 eV could be corresponded to Fe 2p<sub>3/2</sub> and Fe 2p<sub>1/2</sub>,  
109 respectively, which confirmed the existence of Fe<sup>3+</sup> in the M:A=10:1 composite [57]. For the O 1s XPS spectrum  
110 (fig 2D), the peak located at 532.0 eV could be allocated to the O elements of H<sub>2</sub>BDC, while the peak located  
111 at 531.2 eV was belonging to the O elements from Fe—O bonds of Ag<sub>3</sub>PO<sub>4</sub> crystal [58-60]. As for the Ag 3d  
112 spectrum (fig 2E), the peaks located at 368.1 eV and 374.2 eV could be corresponded to Ag 3d<sub>5/2</sub> and Ag 3d<sub>3/2</sub>,  
113 respectively [61]. This confirmed the existence of Ag<sup>+</sup> in M:A=10:1 composite, while the P 2p spectrum (fig  
114 2F) located at 133.6 eV demonstrated the existence of P<sup>5+</sup> in M:A=10:1 composite [62].

115 To analyze the morphology and size of as-prepared samples, scanning electron microscopy (SEM) and  
116 transmission electron microscopy (TEM) characterization methods were carried out. As shown in fig 3A and  
117 3B, MIL-53(Fe) exhibited a nanorod morphology, with the average width and average length being 4-5 and 11-  
118 12 μm, respectively. After the introduction of Ag<sub>3</sub>PO<sub>4</sub> (fig 3C and 3D), the morphology of M:A=10:1 sample  
119 was barely changed, except that the average width of this sample was amplified to 5-6 μm. The yolk-shell  
120 structure of the as-prepared sample could be illustrated by the TEM images. It can be seen from fig 4 that black  
121 Ag<sub>3</sub>PO<sub>4</sub> cores were randomly located, and were covered by the MIL-53(Fe) shell. This structure was conducive  
122 to the improvement of stability of Ag<sub>3</sub>PO<sub>4</sub>, and well protected the Ag<sub>3</sub>PO<sub>4</sub> core from dissolution. The d spacing  
123 value of the lattice fringe, 0.268 nm, was clearly observed in fig 4D, which corresponded to the (210)

124 crystallographic plane of  $\text{Ag}_3\text{PO}_4$ . In addition, the result of energy-dispersive X-ray spectroscopy (EDS) as  
125 shown in fig 3F further confirmed the existence of Ag, Fe and P elements in M:A=10:1 sample. The weight  
126 percentage of Ag was 8.75 wt.% in this composite, which demonstrated that the speculated amount of  $\text{Ag}_3\text{PO}_4$   
127 was introduced into the composite.

128 The nitrogen sorption analysis was used to measure the specific surface area and pore characteristic of  
129 M:A=10:1 sample. As shown in fig 5A, M:A=10:1 sample showed a type IV isothermal with a type  $\text{H}_3$  hysteresis  
130 loop, which demonstrated that a mesopores material was successfully prepared. The Brunauer-Emmett-Teller  
131 (BET) surface area of M:A=10:1 was calculated to be ca.  $397.945 \text{ m}^2/\text{g}$ , which was 11.75 times larger than that  
132 of MIL-53(Fe) (ca.  $33.866 \text{ m}^2/\text{g}$ ). Such expansion of BET surface area could be attributed to the increase in total  
133 pore volume by the introduction of  $\text{Ag}_3\text{PO}_4$ . According to the nitrogen sorption analysis, the total pore volume  
134 of MIL-53(Fe) was  $0.024 \text{ cm}^3/\text{g}$ , while the total pore volume of M:A=10:1 sample was  $0.341 \text{ cm}^3/\text{g}$ . In addition,  
135 the pore size distribution figure (inset in Fig. 5A) shows that a number of pores less than 20 nm are generated,  
136 which further supports our speculation. High specific surface area usually means high adsorption amount and  
137 more surface active sites. Thus it is reasonable to deduce that M:A=10:1 sample possesses better photocatalytic  
138 performance than bare MIL-53(Fe). In addition, the pore size distribution of samples and pore volume data was  
139 depicted in Table 1.

140 UV-vis diffuse reflectance spectra (UV-vis DRS) was applied to evaluate the absorption properties and the  
141 optical bandgap of catalysts. As shown in fig 5B, all the three samples revealed good absorption in the visible  
142 light range ( $< 500 \text{ nm}$ ). After the introduction of  $\text{Ag}_3\text{PO}_4$ , the absorption range of M:A=10:1 was expanded,  
143 which was beneficial to the improvement of photocatalytic activity. Besides, the bandgap edge ( $E_g$ ) of  
144 semiconductors was calculated by the Kubelka-Munk equation (1) [63]:

$$145 \quad \alpha h\nu = A(h\nu - E_g)^{n/2} \quad (1)$$

146 Where  $\alpha$  represents the absorption coefficient,  $\nu$  represents the light frequency,  $E_g$  represents the bandgap energy,  
147 A is a constant, and n depends on the characteristics of the transition in a semiconductor. MIL-53(Fe) is a direct  
148 band semiconductor, while  $\text{Ag}_3\text{PO}_4$  is an indirect transition semiconductor. As presented in Fig 5C and 5D, the  
149 optical bandgap of MIL-53(Fe) and  $\text{Ag}_3\text{PO}_4$  was measured as 1.78 eV and 2.35 eV, respectively.

150 The photocatalytic performance of the samples was assessed by the removal of TC antibiotics. Fig 6A  
151 represents the decomposition rate of TC by different photocatalysts. In blank experiment (no photocatalysts  
152 were added), the TC concentration was barely changed, suggesting that the self-photolysis effect of TC could  
153 be ignored. After the introduction of  $\text{Ag}_3\text{PO}_4$ , the photocatalytic degradation rate was greatly enhanced, which  
154 was in the order of MIL-53(Fe) < M:A=100:1 < M:A=50:1 < M:A=20:1 < M:A=5:1 < M:A=10:1. The pure  
155 MIL-53(Fe) showed the lowest TC removal efficiency (ca. 25.53%) with 1 h visible light irradiation, and  
156 M:A=10:1 sample showed the highest TC removal efficiency (ca. 76.22%) under the same condition, which is  
157 2.98 times than that of pure MIL-53(Fe), and better than that of BiOI [17], g- $\text{C}_3\text{N}_4$  [64, 65],  $\text{WO}_3$  [66],  $\text{BiVO}_4$   
158 [67, 68], CdS [69], and ZnO [70] for the degradation of TC. According to the Langmuir-Hinshelwood kinetic  
159 model, we hypothesized that all the reactions followed the pseudo-first-order model (2):

160 
$$\ln\left(\frac{C_0}{C_t}\right) = kt \times 100\% \quad (2)$$

161 Where k behalf of the apparent reaction rate,  $C_0$  and  $C_t$  presents the TC concentration at beginning and reaction  
162 time t, respectively. The k value of MIL-53(Fe), M:A=100:1, M:A=50:1, M:A=20:1, M:A=10:1, and M:A=50:1  
163 were 0.00219, 0.00184, 0.00359, 0.00441, 0.01232, and 0.01019  $\text{min}^{-1}$ , respectively. Accordingly, the k value  
164 of M:A=10:1 was 5.63 times larger than that of MIL-53(Fe), suggesting that the M:A=10:1 possess the highest  
165 photocatalytic removal efficiency of TC in these samples. The improved photocatalytic activity can be ascribed  
166 to improved migration efficiency of photoinduced carriers. Upon visible light irradiation, the photoinduced  
167 electrons in the CB of  $\text{Ag}_3\text{PO}_4$  could be consumed by the photoinduced holes in the VB of MIL-53(Fe), and

168 holes remained in the VB of  $\text{Ag}_3\text{PO}_4$  would be used in the degradation of pollutants process. Besides,  $\text{Fe}^{3+}$  in  
169 MIL-53(Fe) would react with  $\text{H}_2\text{O}_2$  (generated by  $\text{Ag}_3\text{PO}_4$ ) to yield more reactive species to decompose organic  
170 pollutants. Moreover, adsorption-desorption equilibrium between TC and catalysts was improved by the  
171 introduction of  $\text{Ag}_3\text{PO}_4$ , which was consistent with the BET surface area results.

172 Fig 6B exhibits the TC removal efficiency with different initial concentration of TC using M:A=10:1  
173 sample as photocatalyst, which decreased from 95.18% to 54.61% with the original TC concentration increasing  
174 from 10 to 50 mg/L. Generally, higher initial concentration possesses lower light permeability, which is bad for  
175 the absorption of photons. In addition, intermediates generated from the photocatalysis process would show a  
176 competitive behavior for the limited adsorption and catalytic sites compared to TC, which is bad for the removal  
177 of TC [71]. Thus, the removal rate at high initial TC concentration is much lower than that at low initial TC  
178 concentration. Furthermore, it is worth mentioning that due to the high adsorption amount at 10 mg/L (ca.  
179 70.37%), 20 mg/L initial TC concentration was selected as the baseline in this experiment.

180 The photostability is of great importance to the practical applications. Fig 6C shows the five time cycling  
181 experiment by using  $\text{Ag}_3\text{PO}_4$  and M:A=10:1 as catalysts. It can be seen that the removal efficiency of bare  
182  $\text{Ag}_3\text{PO}_4$  for TC was greatly degraded from 78.67% to 34.46% after five time run. However, only 6.09% losses  
183 at the three runs were detected in the M:A=10:1 sample (from 76.22% to 70.13%), and remain 55.84% after  
184 five runs. This is manifested that the MOF shell play a vital role to protect the  $\text{Ag}_3\text{PO}_4$  core from photocorrosion.  
185 The XRD pattern of M:A=10:1 sample after five runs (Fig 1A) shows almost the same pattern that the original  
186 M:A=10:1 sample, while the peak at  $38.1^\circ$  could ascribed to the  $\text{Ag}^0$  (marked with ※) particles that produced  
187 from photocorrosion of  $\text{Ag}_3\text{PO}_4$ . This characterization results also proved that this hybrid has a stable structure.

188 Photoluminescence (PL) spectra was applied to reveal the separation efficiency of photogenerated carriers  
189 in photocatalysts [71, 72]. Fig 7A shows the PL spectra of pure MIL-53(Fe),  $\text{Ag}_3\text{PO}_4$ , and M:A=10:1 samples

190 (excitation wavelength: 437 nm). The PL intensities were shown as follows: MIL-53(Fe) > Ag<sub>3</sub>PO<sub>4</sub> > M:A=10:1.  
191 In general, the higher PL signal, the lower separation efficiency of photogenerated carriers. Thus, both bare  
192 MIL-53(Fe) and Ag<sub>3</sub>PO<sub>4</sub> presented a relatively high recombination rate of photogenerated carriers, and  
193 M:A=10:1 sample possesses the lowest recombination rate among these three photocatalysts. This agrees well  
194 with the result of TC degradation experiment. The PL results indicated that the import of Ag<sub>3</sub>PO<sub>4</sub> into MIL-  
195 53(Fe) could effectively promote the separation efficiency of photoinduced carriers, thus enhancing the  
196 photocatalytic activity. The highest intensity could be attributed to the efficient charge transfer and separation  
197 process, which are contributed to the yolk-shell heterostructure between Ag<sub>3</sub>PO<sub>4</sub> and MIL-53(Fe).

198 Photocurrent response and electrochemical impedance spectra (EIS) was used for further investigation of  
199 charge separation and migration behavior of catalysts. As presented in fig 7B, photocurrent intensity of pure  
200 MIL-53(Fe) was barely observed, while pure Ag<sub>3</sub>PO<sub>4</sub> showed relatively lower photocurrent intensity contrast  
201 to M:A=10:1 sample. In fact, photocurrent intensity of M:A=10:1 was about 1.53 times and 9.2 times higher  
202 than that of Ag<sub>3</sub>PO<sub>4</sub> and MIL-53(Fe), respectively. As depicted in fig 7C, the semicircular diameter of these  
203 tested samples was in the sequence of MIL-53(Fe) > Ag<sub>3</sub>PO<sub>4</sub> > M:A=10:1. Normally, a smaller arc radius of  
204 the Nyquist plots in EIS test means a smaller charge transfer resistance ( or a higher efficiency in charge transfer)  
205 [73]. Hence, M:A=10:1 sample showed the highest efficiency in charge transfer among these three samples,  
206 which were in consistent with the above-discussed results.

207 To evidence the H<sub>2</sub>O<sub>2</sub> generated by Ag<sub>3</sub>PO<sub>4</sub> could be decomposed by the introduction of MIL-53(Fe), a  
208 permanganate titration was used to detect the concentration of H<sub>2</sub>O<sub>2</sub> for M:A=10:1 and Ag<sub>3</sub>PO<sub>4</sub> upon visible  
209 light irradiation. As displayed in fig 7D, it can be clearly observed that for pure Ag<sub>3</sub>PO<sub>4</sub>, the concentration of  
210 H<sub>2</sub>O<sub>2</sub> could reach to 154 μmol/L, while for M:A=10:1 sample, the detected H<sub>2</sub>O<sub>2</sub> concentration is 52 μmol/L.  
211 This results indicated that a big part of generated H<sub>2</sub>O<sub>2</sub> on the Ag<sub>3</sub>PO<sub>4</sub> core would be quickly decomposed by

212 the MIL-53(Fe) shell, which reduces the consumption of holes (from  $\text{Ag}_3\text{PO}_4$ ) as well as generates more reactive  
213 species (through photo-Fenton-like reaction) to react with target pollutants.

214 The introduction of  $\text{Ag}_3\text{PO}_4$  as a core into the MIL-53(Fe) shell could effectively suppress the  
215 recombination of photoinduced electron-hole pairs. To explore the dominant reactive species in this reaction,  
216 three types of chemicals, BQ,  $\text{Na}_2\text{C}_2\text{O}_4$  and IPA were used to trap  $\text{O}_2^-$  radicals,  $\text{h}^+$  radicals, and  $\text{OH}$  radicals,  
217 respectively [47, 74, 75]. As depicted in fig 8A, when  $\text{Na}_2\text{C}_2\text{O}_4$  and BQ were added in this system, the  
218 degradation rate decreased from 76.22% to 48.34% and 53.32%, respectively. The addition of IPA also had an  
219 influence on the removal efficiency of TC, but only 10.14% of reduction was measured. The above results  
220 suggested that the  $\text{h}^+$  and  $\text{O}_2^-$  were the predominant reactive species for the TC removal by M:A=10:1 samples.

221 To further confirm the trapping experiment results, the electron spin resonance (ESR) technique was  
222 carried out. DMPO was used to capture the  $\text{O}_2^-$  and  $\text{OH}$  radicals, while TEMPO was used to capture the  $\text{h}^+$   
223 radicals. As displayed in fig 8B and 8C, no signals in dark condition were observed in both ESR spectra, whereas  
224 four characteristic peaks of DMPO- $\text{O}_2^-$  and DMPO- $\text{OH}$  were detected after the light turns on. As the irradiation  
225 time increases, the peak intensity also increased. This demonstrated the existence of  $\text{O}_2^-$  and  $\text{OH}$  radicals in  
226 this system. Furthermore, as presented in fig 8D, three strong characteristic peaks of TEMPO- $\text{h}^+$  were detected  
227 in both dark and visible light condition. In addition, the peak intensity increased with the irradiation time goes  
228 on, which verified that the  $\text{h}^+$  radicals also worked in this system.

229 In general, the high photocatalytic performance of yolk-shell  $\text{Ag}_3\text{PO}_4@\text{MIL-53(Fe)}$  catalyst could be  
230 attributed to the high surface area, absorption capability and separation efficiency of photoinduced charge  
231 carriers. Based on the above-experimental results, the possible photocatalytic mechanism in  $\text{Ag}_3\text{PO}_4@\text{MIL-}$   
232  $53(\text{Fe})$  yolk-shell structure composites was depicted in fig 9.  $\text{Ag}_3\text{PO}_4$  particles were randomly located in the  
233 cavities of MIL-53(Fe) shell. As long as visible light irradiation started, both  $\text{Ag}_3\text{PO}_4$  and MIL-53(Fe) could be

234 activated to yield electrons and holes, and the photoinduced electrons in the CB of Ag<sub>3</sub>PO<sub>4</sub> could be depleted  
235 by the photoinduced h<sup>+</sup> in the VB of MIL-53(Fe). Hence, the separation efficiency increased. Holes remained  
236 in the VB of Ag<sub>3</sub>PO<sub>4</sub> could take part in the degradation of pollutants process. Besides, a small part of the  
237 remained electrons in the CB of Ag<sub>3</sub>PO<sub>4</sub> could be transferred into H<sub>2</sub>O<sub>2</sub>, which may restrain the photocatalytic  
238 activity of Ag<sub>3</sub>PO<sub>4</sub> (H<sub>2</sub>O<sub>2</sub> + 2h<sup>+</sup>(Ag<sub>3</sub>PO<sub>4</sub>) → O<sub>2</sub> + 2H<sup>+</sup>). Thus, when the Ag<sub>3</sub>PO<sub>4</sub> cores were covered by MIL-  
239 53(Fe) shell, the generated H<sub>2</sub>O<sub>2</sub> could be consumed via a photo-Fenton-like reaction:



245 In addition, the stability of Ag<sub>3</sub>PO<sub>4</sub> could be increased by the protection shell of MIL-53(Fe), which makes a  
246 big step forward for its practice application

#### 247 4. Conclusions

248 In this work, we successfully synthesized a yolk-shell Ag<sub>3</sub>PO<sub>4</sub>@MIL-53(Fe) Z-scheme photocatalyst via  
249 a “bottle-around-ship” like method, which exhibited enlarged BET surface area and superior photocatalytic  
250 performance for TC removal upon visible light irradiation. The increased BET surface area is attributed to the  
251 introduction of Ag<sub>3</sub>PO<sub>4</sub> makes the porosity of hybrids greatly improved. The total pore volume of MIL-53(Fe)  
252 is 0.024 cm<sup>3</sup>/g, while after the introduction of Ag<sub>3</sub>PO<sub>4</sub> cores, the total pore volume was enlarged to 0.341 cm<sup>3</sup>/g,  
253 both the BET surface area and total pore volume are far more than the Ag<sub>3</sub>PO<sub>4</sub>/MIL-53(Fe) composite that Xie  
254 et al. reported [39]. As is well-known, high specific surface area usually means high adsorption amount and  
255 more surface active sites, which is conducive to improve the photocatalytic performance. In addition, the

256 boosted photocatalytic performance was mainly ascribed to the Z-scheme structure which consumed the  
257 photogenerated  $e^-(\text{Ag}_3\text{PO}_4)$  and  $h^+(\text{MIL-53}(\text{Fe}))$ , leading to more  $h^+(\text{Ag}_3\text{PO}_4)$  and  $e^-(\text{MIL-53}(\text{Fe}))$  participate  
258 in the photocatalytic procedure. Moreover, this hybrid composites subtly took advantage of MIL-53(Fe) for a  
259 photo-Fenton-like reaction to decompose the unwanted  $\text{H}_2\text{O}_2$  (generated by  $\text{Ag}_3\text{PO}_4$ ), which not only restrained  
260 the meaningless consumption of  $h^+(\text{Ag}_3\text{PO}_4)$ , but also generated more reactive species ( $h^+$  and  $\cdot\text{OH}$ ) to take part  
261 in the photocatalytic reaction. Besides, the yolk-shell structure was conducive to inhibit the dissolution of  
262  $\text{Ag}_3\text{PO}_4$ , thereby improving its stability. This study offers a simple way to design and fabricate yolk-shell  
263 structure photocatalysts with large surface area and excellent photocatalytic performance for environmental  
264 remediation.

## 265 Acknowledgements

266 The study is financially supported by the Program for the National Natural Science Foundation of China  
267 (51521006, 51508178, 51779089, 51709101, and 51508177) and the Program for Changjiang Scholars and  
268 Innovative Research Team in University (IRT-15R17).

## 269 References

- 270 [1] J.-L. Gong, B. Wang, G. M. Zeng, C. P. Yang, C.-G. Niu, Q.-Y. Niu, W.-J. Zhou, Y. Liang, Removal of cationic  
271 dyes from aqueous solution using magnetic multi-wall carbon nanotube nanocomposite as adsorbent, *Journal of*  
272 *Hazardous Materials* 164(2) (2009) 1517-1522.
- 273 [2] P. Xu, G.M. Zeng, D.L. Huang, C.L. Feng, S. Hu, M.H. Zhao, C. Lai, Z. Wei, C. Huang, G.X. Xie, Z.F. Liu, Use of iron  
274 oxide nanomaterials in wastewater treatment: A review, *Science of The Total Environment* 424 (2012) 1-10.
- 275 [3] K. He, G. Chen, G. Zeng, A. Chen, Z. Huang, J. Shi, T. Huang, M. Peng, L. Hu, Three-dimensional graphene  
276 supported catalysts for organic dyes degradation, *Applied Catalysis B: Environmental* 228 (2018) 19-28.
- 277 [4] Y. Wang, Y. Zhu, Y. Hu, G. Zeng, Y. Zhang, C. Zhang, C. Feng, How to Construct DNA Hydrogels for Environmental  
278 Applications: Advanced Water Treatment and Environmental Analysis, *Small* 14(17) (2018) 1703305.
- 279 [5] X. Tang, G. Zeng, C. Fan, M. Zhou, L. Tang, J. Zhu, J. Wan, D. Huang, M. Chen, P. Xu, C. Zhang, Y. Lu, W. Xiong,  
280 Chromosomal expression of CadR on *Pseudomonas aeruginosa* for the removal of Cd(II) from aqueous solutions,  
281 *Science of The Total Environment* 636 (2018) 1355-1361.
- 282 [6] S. Ye, G. Zeng, H. Wu, C. Zhang, J. Liang, J. Dai, Z. Liu, W. Xiong, J. Wan, P. Xu, M. Cheng, Co-occurrence and  
283 interactions of pollutants, and their impacts on soil remediation—A review, 47 (2017) 1528-1553.
- 284 [7] L. Qin, G. Zeng, C. Lai, D. Huang, P. Xu, C. Zhang, M. Cheng, X. Liu, S. Liu, B. Li, H. Yi, "Gold rush" in modern  
285 science: Fabrication strategies and typical advanced applications of gold nanoparticles in sensing, *Coordination*

286 Chemistry Reviews 359 (2018) 1-31.

287 [8] S. Ye, G. Zeng, H. Wu, C. Zhang, J. Dai, J. Liang, J. Yu, X. Ren, H. Yi, M. Cheng, C. Zhang, Biological technologies  
288 for the remediation of co-contaminated soil, *Critical Reviews in Biotechnology* 37(8) (2017) 1062-1076.

289 [9] B. Song, M. Chen, S. Ye, P. Xu, G. Zeng, J. Gong, J. Li, P. Zhang, W. Cao, Effects of multi-walled carbon nanotubes  
290 on metabolic function of the microbial community in riverine sediment contaminated with phenanthrene, *Carbon*  
291 144 (2019) 1-7.

292 [10] H. Yi, M. Jiang, D. Huang, G. Zeng, C. Lai, L. Qin, C. Zhou, B. Li, X. Liu, M. Cheng, W. Xue, P. Xu, C. Zhang,  
293 Advanced photocatalytic Fenton-like process over biomimetic hemin-Bi<sub>2</sub>WO<sub>6</sub> with enhanced pH, *Journal of the*  
294 *Taiwan Institute of Chemical Engineers* 93 (2018) 184-192.

295 [11] S. Li, W. Shi, W. Liu, H. Li, W. Zhang, J. Hu, Y. Ke, W. Sun, J. Ni, A duodecennial national synthesis of antibiotics  
296 in China's major rivers and seas (2005-2016), *The Science of the total environment* 615 (2018) 906-917.

297 [12] Y. Deng, L. Tang, G. Zeng, J. Wang, Y. Zhou, J. Wang, J. Tang, L. Wang, C. Feng, Facile fabrication of mediator-  
298 free Z-scheme photocatalyst of phosphorous-doped ultrathin graphitic carbon nitride nanosheets and bismuth  
299 vanadate composites with enhanced tetracycline degradation under visible light, *Journal of Colloid & Interface*  
300 *Science* 509 (2017) 219.

301 [13] J.A. Park, A. Nam, J.H. Kim, S.T. Yun, J.W. Choi, S.H. Lee, Blend-electrospun graphene oxide/Poly(vinylidene  
302 fluoride) nanofibrous membranes with high flux, tetracycline removal and anti-fouling properties, *Chemosphere*  
303 207 (2018) 347.

304 [14] X. Zhu, Y. Liu, F. Qian, C. Zhou, S. Zhang, J. Chen, Preparation of magnetic porous carbon from waste hydrochar  
305 by simultaneous activation and magnetization for tetracycline removal, *Bioresour Technol* 154(2) (2014) 209-214.

306 [15] B. Kakavandi, A. Takdastan, N. Jaafarzadeh, M. Azizi, A. Mirzaei, A. Azari, Application of Fe<sub>3</sub>O<sub>4</sub>@C catalyzing  
307 heterogeneous UV-Fenton system for tetracycline removal with a focus on optimization by a response surface  
308 method, *Journal of Photochemistry and Photobiology A: Chemistry* 314 (2016) 178-188.

309 [16] D. Wang, F. Jia, H. Wang, F. Chen, Y. Fang, W. Jiang, G. Zeng, X. Li, Q. Yang, X. Yuan, efficient adsorption and  
310 photocatalytic degradation of tetracycline by Fe-based MOFs, *Journal of Colloid & Interface Science* 519 (2018)  
311 273.

312 [17] Y. Yang, Z. Zeng, Z. Chen, D. Huang, G. Zeng, X. Rong, L. Cui, C. Zhou, G. Hai, W. Xue, Construction of iodine  
313 vacancy-rich BiOI/Ag@AgI Z-scheme heterojunction photocatalysts for visible-light-driven tetracycline  
314 degradation: transformation pathways and mechanism insight, *Chemical Engineering Journal* (2018)  
315 S1385894718309069.

316 [18] C. Zhou, C. Lai, P. Xu, G. Zeng, D. Huang, Z. Li, C. Zhang, M. Cheng, L. Hu, J. Wan, Rational Design of Carbon-  
317 Doped Carbon Nitride/Bi<sub>12</sub>O<sub>17</sub>Cl<sub>2</sub> Composites: A Promising Candidate Photocatalyst for Boosting Visible-Light-  
318 Driven Photocatalytic Degradation of Tetracycline, *Sustainable Chemistry & Engineering*, 2018, 6(3) 4174-4184.

319 [19] L. Jiang, X. Yuan, G. Zeng, Z. Wu, J. Liang, X. Chen, L. Leng, H. Wang, H. Wang, Metal-free efficient photocatalyst  
320 for stable visible-light photocatalytic degradation of refractory pollutant, *Applied Catalysis B Environmental* 221  
321 (2017) 715-725.

322 [20] W. Hou, X. Yuan, W. Yan, G. Zeng, H. Dong, X. Chen, L. Leng, Z. Wu, L. Peng, In situ synthesis of In<sub>2</sub>S<sub>3</sub>@MIL-  
323 125(Ti) core-shell microparticle for the removal of tetracycline from wastewater by integrated adsorption and  
324 visible-light-driven photocatalysis, *Applied Catalysis B Environmental* 186 (2016) 19-29.

325 [21] Y. Yang, C. Zhang, C. Lai, G. Zeng, D. Huang, M. Cheng, J. Wang, F. Chen, C. Zhou, W. Xiong, BiOX (X = Cl, Br,  
326 I) photocatalytic nanomaterials: Applications for fuels and environmental management, *Advances in Colloid &*  
327 *Interface Science* (2018) 19-29.

328 [22] C. Zhou, C. Lai, C. Zhang, G. Zeng, D. Huang, M. Cheng, L. Hu, W. Xiong, M. Chen, J. Wang, Y. Yang, L. Jiang,  
329 Semiconductor/boron nitride composites: Synthesis, properties, and photocatalysis applications, *Applied Catalysis*

330 B: Environmental 238 (2018) 6-18.

331 [23] S. Ye, M. Yan, X. Tan, J. Liang, G. Zeng, H. Wu, B. Song, C. Zhou, Y. Yang, H. Wang, Facile assembled biochar-  
332 based nanocomposite with improved graphitization for efficient photocatalytic activity driven by visible light,  
333 Applied Catalysis B: Environmental 250 (2019) 78-88.

334 [24] H. Yi, M. Yan, D. Huang, G. Zeng, C. Lai, M. Li, X. Huo, L. Qin, S. Liu, X. Liu, B. Li, H. Wang, M. Shen, Y. Fu, X. Guo,  
335 Synergistic effect of artificial enzyme and 2D nano-structured Bi<sub>2</sub>WO<sub>6</sub> for eco-friendly and efficient biomimetic  
336 photocatalysis, Applied Catalysis B: Environmental 250 (2019) 52-62.

337 [25] H. Wang, Z. Zeng, P. Xu, L. Li, G. Zeng, R. Xiao, Z. Tang, D. Huang, L. Tang, C. Lai, D. Jiang, Y. Liu, H. Yi, L. Qin,  
338 S. Ye, X. Ren, W. Tang, Recent progress in covalent organic framework thin films: fabrications, applications and  
339 perspectives, Chemical Society Reviews 48(2) (2019) 488-516.

340 [26] D. Jiang, M. Chen, H. Wang, G. Zeng, D. Huang, M. Cheng, Y. Liu, W. Xue, Z. Wang, The application of different  
341 topological and structural MOFs-based materials for the dyes adsorption, Coordination Chemistry Reviews 380  
342 (2019) 471-483.

343 [27] B. Li, H.M. Wen, Y. Cui, W. Zhou, G. Qian, B. Chen, Emerging Multifunctional Metal-Organic Framework  
344 Materials, Advanced Materials 28(40) (2016) 8819-8860.

345 [28] E. Haque, J.W. Jun, S.H. Jhung, Adsorptive removal of methyl orange and methylene blue from aqueous solution  
346 with a metal-organic framework material, iron terephthalate (MOF-235), Journal of Hazardous Materials 185(1)  
347 (2011) 507-511.

348 [29] M. Anbia, V. Hoseini, S. Sheykhi, Sorption of methane, hydrogen and carbon dioxide on metal-organic  
349 framework, iron terephthalate (MOF-235), Journal of Industrial & Engineering Chemistry 18(3) (2012) 1149-1152.

350 [30] W. Xiong, Z. Zeng, X. Li, G. Zeng, R. Xiao, Z. Yang, Y. Zhou, C. Zhang, M. Cheng, L. Hu, C. Zhou, L. Qin, R. Xu,  
351 Y. Zhang, Multi-walled carbon nanotube/amino-functionalized MIL-53(Fe) composites: Remarkable adsorptive  
352 removal of antibiotics from aqueous solutions, Chemosphere 210 (2018) 1061-1069.

353 [31] W. Xiong, G. Zeng, Z. Yang, Y. Zhou, C. Zhang, M. Cheng, Y. Liu, L. Hu, J. Wan, C. Zhou, R. Xu, X. Li, Adsorption  
354 of tetracycline antibiotics from aqueous solutions on nanocomposite multi-walled carbon nanotube functionalized  
355 MIL-53(Fe) as new adsorbent, Science of The Total Environment 627 (2018) 235-244.

356 [32] X. Li, P. Xu, M. Chen, G. Zeng, D. Wang, G. Chen, W. Tang, C. Chen, C. Zhang, X. Tan, Application of silver  
357 phosphate-based photocatalysts: Barrier and solutions, Chemical Engineering Journal 366 (2019) 339-357.

358 [33] L. Zhang, J. Zhang, G. Zeng, C. Dong, Y. Chen, C. Huang, Y. Zhu, R. Xu, Y. Cheng, K. Hou, W. Cao, W. Fang,  
359 Multivariate relationships between microbial communities and environmental variables during co-composting of  
360 sewage sludge and agricultural waste in the presence of PVP-AgNPs, Bioresource Technology 261 (2018) 10-18.

361 [34] K. He, Z. Zeng, A. Chen, G. Zeng, R. Xiao, P. Xu, Z. Huang, J. Shi, L. Hu, G. Chen, Advancement of Ag-Graphene  
362 Based Nanocomposites: An Overview of Synthesis and Its Applications, Small 14(32) (2018) 1800871.

363 [35] Z. Huang, K. He, Z. Song, G. Zeng, A. Chen, L. Yuan, H. Li, L. Hu, Z. Guo, G. Chen, Antioxidative response of  
364 Phanerochaete chrysosporium against silver nanoparticle-induced toxicity and its potential mechanism,  
365 Chemosphere 211 (2018) 573-583.

366 [36] G. Li, S. Zhao, Y. Zhang, Z. Tang, Metal-Organic Frameworks Encapsulating Active Nanoparticles as Emerging  
367 Composites for Catalysis: Recent Progress and Perspectives, Adv Mater 30(51) (2018) e1800702.

368 [37] S. Mosleh, M.R. Rahimi, M. Ghaedi, K. Dashtian, Sonophotocatalytic degradation of trypan blue and vesuvine  
369 dyes in the presence of blue light active photocatalyst of Ag<sub>3</sub>PO<sub>4</sub>/Bi<sub>2</sub>S<sub>3</sub>-HKUST-1-MOF: Central composite  
370 optimization and synergistic effect study, Ultrasonics Sonochemistry 32 (2016) 387-397.

371 [38] S. Mosleh, M.R. Rahimi, M. Ghaedi, K. Dashtian, S. Hajati, S. Wang, Ag<sub>3</sub>PO<sub>4</sub>/AgBr/Ag-HKUST-1-MOF  
372 composites as novel blue LED light active photocatalyst for enhanced degradation of ternary mixture of dyes in a  
373 rotating packed bed reactor, Chemical Engineering and Processing: Process Intensification 114 (2017) 24-38.

374 [39] X.-Y. Xu, C. Chu, H. Fu, X.-D. Du, P. Wang, W. Zheng, C.-C. Wang, Light-responsive UiO-66-NH<sub>2</sub>/Ag<sub>3</sub>PO<sub>4</sub>  
375 MOF-nanoparticle composites for the capture and release of sulfamethoxazole, *Chemical Engineering Journal* 350  
376 (2018) 436-444.

377 [40] F.A. Sofi, K. Majid, O. Mehraj, The visible light driven copper based metal-organic-framework  
378 heterojunction:HKUST-1@Ag-Ag<sub>3</sub>PO<sub>4</sub> for plasmon enhanced visible light photocatalysis, *Journal of Alloys and*  
379 *Compounds* 737 (2018) 798-808.

380 [41] T. Zhou, G. Zhang, H. Zhang, H. Yang, P. Ma, X. Li, X. Qiu, G. Liu, Highly efficient visible-light-driven  
381 photocatalytic degradation of rhodamine B by a novel Z-scheme Ag<sub>3</sub>PO<sub>4</sub>/MIL-101/NiFe<sub>2</sub>O<sub>4</sub> composite, *Catalysis*  
382 *Science & Technology* 8(9) (2018) 2402-2416.

383 [42] X. Qian, H. Xu, X. Zhang, R. Lei, J. Gao, S. Xu, Enhanced visible-light-driven photocatalytic activity of  
384 Ag<sub>3</sub>PO<sub>4</sub>/metal-organic framework composite, *Polyhedron* 163 (2019) 1-6.

385 [43] R.A. Rather, Z.N. Siddiqui, Silver phosphate supported on metal-organic framework (Ag<sub>3</sub>PO<sub>4</sub>@MOF-5) as a  
386 novel heterogeneous catalyst for green synthesis of indenoquinolinediones, *Applied Organometallic Chemistry* 0(0)  
387 (2019) e5176.

388 [44] H. Katsumata, M. Taniguchi, S. Kaneco, T. Suzuki, Photocatalytic degradation of bisphenol A by Ag<sub>3</sub>PO<sub>4</sub>  
389 under visible light, *Catalysis Communications* 34(13) (2013) 30-34.

390 [45] S. Huang, Y. Xua, T. Zhou, X. Meng, M. Yun, Q. Liua, L. Jinga, X. Hua, H. Li, Constructing magnetic catalysts  
391 with in-situ solid-liquid interfacial photo-Fenton-like reaction over Ag<sub>3</sub>PO<sub>4</sub>@NiFe<sub>2</sub>O<sub>4</sub> composites, *Applied*  
392 *Catalysis B Environmental* 225 (2017).

393 [46] S. Huang, Y. Xu, T. Zhou, M. Xie, Y. Ma, Q. Liu, L. Jing, H. Xu, H. Li, Constructing magnetic catalysts with in-situ  
394 solid-liquid interfacial photo-Fenton-like reaction over Ag<sub>3</sub>PO<sub>4</sub>@NiFe<sub>2</sub>O<sub>4</sub> composites, *Applied Catalysis B:*  
395 *Environmental* 225 (2018) 40-50.

396 [47] L. Xie, Z. Yang, W. Xiong, Y. Zhou, J. Cao, Y. Peng, X. Li, C. Zhou, R. Xu, Y. Zhang, Construction of MIL-53(Fe)  
397 metal-organic framework modified by silver phosphate nanoparticles as a novel Z-scheme photocatalyst: Visible-  
398 light photocatalytic performance and mechanism investigation, *Applied Surface Science*, 465 (2019) 103-115.

399 [48] F. Millange, N. Guillou, R.I. Walton, J.M. Greer, M. Margiolaki, G. Férey, Effect of the nature of the metal on  
400 the breathing steps in MOFs with dynamic frameworks, *Chemical Communications* 39(39) (2008) 4732-4734.

401 [49] Y. Zhiguo, Y. Jinhua, K. Naoki, K. Takuya, D. Shuxin, S.W. Hilary, Y. Hui, C. Junyu, L. Wenjun, L. Zhaosheng, An  
402 orthophosphate semiconductor with photooxidation properties under visible-light irradiation, *Nature Materials* 9(7)  
403 (2010) 559-564.

404 [50] L. Ai, C. Zhang, L. Li, J. Jing, Iron terephthalate metal-organic framework: Revealing the effective activation of  
405 hydrogen peroxide for the degradation of organic dye under visible light irradiation, *Applied Catalysis B*  
406 *Environmental* 148-149(1) (2014) 191-200.

407 [51] C. Zhang, L. Ai, J. Jing, Graphene Hybridized Photoactive Iron Terephthalate with Enhanced Photocatalytic  
408 Activity for the Degradation of Rhodamine B under Visible Light, *Industrial & Engineering Chemistry Research* 54(1)  
409 (2015) 153-163.

410 [52] A. Banerjee, R. Gokhale, S. Bhatnagar, J. Jog, M. Bhardwaj, B. Lefez, B. Hannoyer, S. Ogale, MOF derived porous  
411 carbon-Fe<sub>3</sub>O<sub>4</sub> nanocomposite as a high performance, recyclable environmental superadsorbent, *Journal of*  
412 *Materials Chemistry* 22(37) (2012) 19694-19699.

413 [53] P. Horcajada, C. Serre, G. Maurin, N.A. Ramsahye, F. Balas, M. Valletregí, M. Sebban, F. Taulelle, G. Férey, Flexible  
414 Porous Metal-Organic Frameworks for a Controlled Drug Delivery, *Journal of the American Chemical Society* 130(21)  
415 (2008) 6774-6780.

416 [54] C. Gong, D. Chen, X. Jiao, Q. Wang, Continuous hollow  $\alpha$ -Fe<sub>2</sub>O<sub>3</sub> and  $\alpha$ -Fe fibers prepared by the sol-gel  
417 method, *Journal of Materials Chemistry* 12(6) (2002) 1844-1847.

418 [55] C. Tao, Y. Liu, L. Wang, S. Zhang, Y. Zeng, J. Yuan, J. Ma, W. Dong, C. Liu, S. Luo, Silver phosphate-based Z-  
419 Scheme photocatalytic system with superior sunlight photocatalytic activities and anti-photocorrosion performance,  
420 Applied Catalysis B Environmental 208(Complete) (2017) 1-13.

421 [56] S.K. Tam, D. Julie, P. Stefania, M. Martin, H. Jean-Pierre, Y. L'Hocine, Physicochemical model of alginate-poly-  
422 L-lysine microcapsules defined at the micrometric/nanometric scale using ATR-FTIR, XPS, and ToF-SIMS,  
423 Biomaterials 26(34) (2005) 6950-6961.

424 [57] C. Yu, L. Gou, X. Zhou, N. Bao, H. Gu, Chitosan-Fe<sub>3</sub>O<sub>4</sub> nanocomposite based electrochemical sensors for the  
425 determination of bisphenol A, Electrochimica Acta 56(25) (2011) 9056-9063.

426 [58] T. Yan, J. Tian, W. Guan, Q. Zheng, W. Li, J. You, B. Huang, Ultra-low loading of Ag<sub>3</sub>PO<sub>4</sub> on hierarchical In<sub>2</sub>S<sub>3</sub>  
427 microspheres to improve the photocatalytic performance: The cocatalytic effect of Ag and Ag<sub>3</sub>PO<sub>4</sub>, Applied  
428 Catalysis B Environmental 202 (2017) 84-94.

429 [59] R. Liang, F. Jing, L. Shen, N. Qin, L. Wu, MIL-53(Fe) as a highly efficient bifunctional photocatalyst for the  
430 simultaneous reduction of Cr(VI) and oxidation of dyes, Journal of Hazardous Materials 287 (2015) 364-372.

431 [60] C. Vimlesh, P. Jaesung, C. Young, L. Jung Woo, H. In-Chul, K.S. Kim, Water-dispersible magnetite-reduced  
432 graphene oxide composites for arsenic removal, Acs Nano 4(7) (2010) 3979-3986.

433 [61] L. Zhou, W. Zhang, L. Chen, H. Deng, Z-scheme mechanism of photogenerated carriers for hybrid photocatalyst  
434 Ag<sub>3</sub>PO<sub>4</sub>/g-C<sub>3</sub>N<sub>4</sub> in degradation of sulfamethoxazole, Journal of Colloid & Interface Science 487 (2017) 410-  
435 417.

436 [62] R. Zheng, L. Li, J. Xie, Y. Zhu, Y. Xie, State of Doped Phosphorus and Its Influence on the Physicochemical and  
437 Photocatalytic Properties of P-doped Titania, Journal of Physical Chemistry C 112(39) (2008) 15502-15509.

438 [63] C. Fei, Y. Qi, Y. Wang, J. Zhao, D. Wang, X. Li, G. Zhi, W. Hou, Y. Deng, C. Niu, Novel ternary heterojunction  
439 photocatalyst of Ag nanoparticles and g-C<sub>3</sub>N<sub>4</sub> nanosheet TiO<sub>2</sub>-modified BiVO<sub>4</sub> for wider spectrum visible-light  
440 photocatalytic degradation of refractory pollutant, Applied Catalysis B Environmental 205 (2016) 133-147.

441 [64] Y. Yang, C. Zhang, D. Huang, G. Zeng, J. Huang, C. Lai, C. Zhou, W. Wang, H. Guo, W. Xue, R. Deng, M. Cheng,  
442 W. Xiong, Boron nitride quantum dots decorated ultrathin porous g-C<sub>3</sub>N<sub>4</sub>: Intensified exciton dissociation and  
443 charge transfer for promoting visible-light-driven molecular oxygen activation, Applied Catalysis B: Environmental  
444 245 (2019) 87-99.

445 [65] W. Wang, P. Xu, M. Chen, G. Zeng, C. Zhang, C. Zhou, Y. Yang, D. Huang, C. Lai, M. Cheng, L. Hu, W. Xiong, H.  
446 Guo, M. Zhou, Alkali Metal-Assisted Synthesis of Graphite Carbon Nitride with Tunable Band-Gap for Enhanced  
447 Visible-Light-Driven Photocatalytic Performance, ACS Sustainable Chemistry & Engineering 6(11) (2018) 15503-  
448 15516.

449 [66] T. Xiao, Z. Tang, Y. Yang, L. Yang, Y. Zhou, Z. Zou, In situ construction of hierarchical WO<sub>3</sub>/g-C<sub>3</sub>N<sub>4</sub> composite  
450 hollow microspheres as a Z-scheme photocatalyst for the degradation of antibiotics, Applied Catalysis B:  
451 Environmental 220 (2018) 417-428.

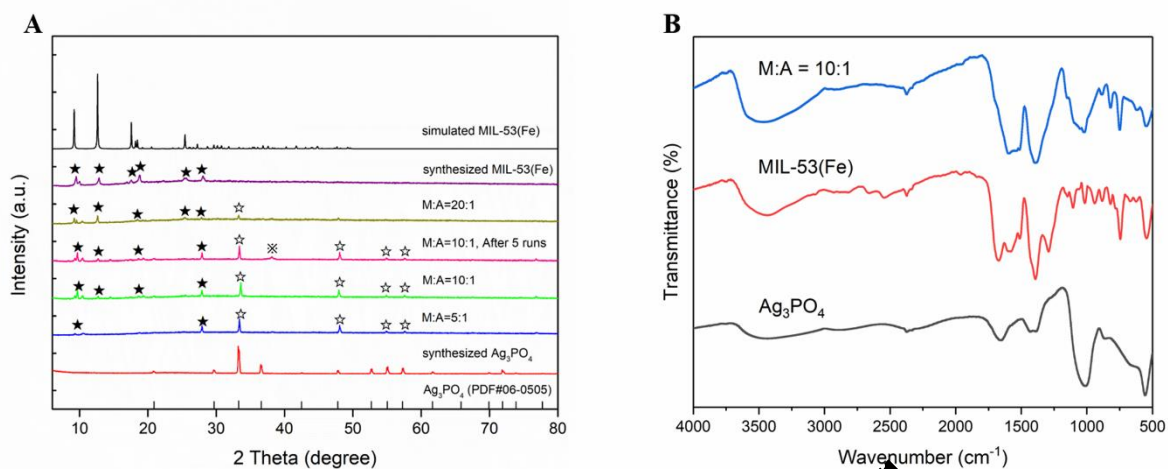
452 [67] Y. Liu, J. Kong, J. Yuan, W. Zhao, X. Zhu, C. Sun, J. Xie, Enhanced photocatalytic activity over flower-like sphere  
453 Ag/Ag<sub>2</sub>CO<sub>3</sub>/BiVO<sub>4</sub> plasmonic heterojunction photocatalyst for tetracycline degradation, Chemical Engineering  
454 Journal 331 (2018) 242-254.

455 [68] Y. Deng, L. Tang, G. Zeng, J. Wang, Y. Zhou, J. Wang, J. Tang, L. Wang, C. Feng, Facile fabrication of mediator-  
456 free Z-scheme photocatalyst of phosphorous-doped ultrathin graphitic carbon nitride nanosheets and bismuth  
457 vanadate composites with enhanced tetracycline degradation under visible light, Journal of Colloid and Interface  
458 Science 509 (2018) 219-234.

459 [69] Y. Feng, X. Yan, C. Liu, Y. Hong, L. Zhu, M. Zhou, W. Shi, Hydrothermal synthesis of CdS/Bi<sub>2</sub>MoO<sub>6</sub> heterojunction  
460 photocatalysts with excellent visible-light-driven photocatalytic performance, Applied Surface Science 353 (2015)  
461 87-94.

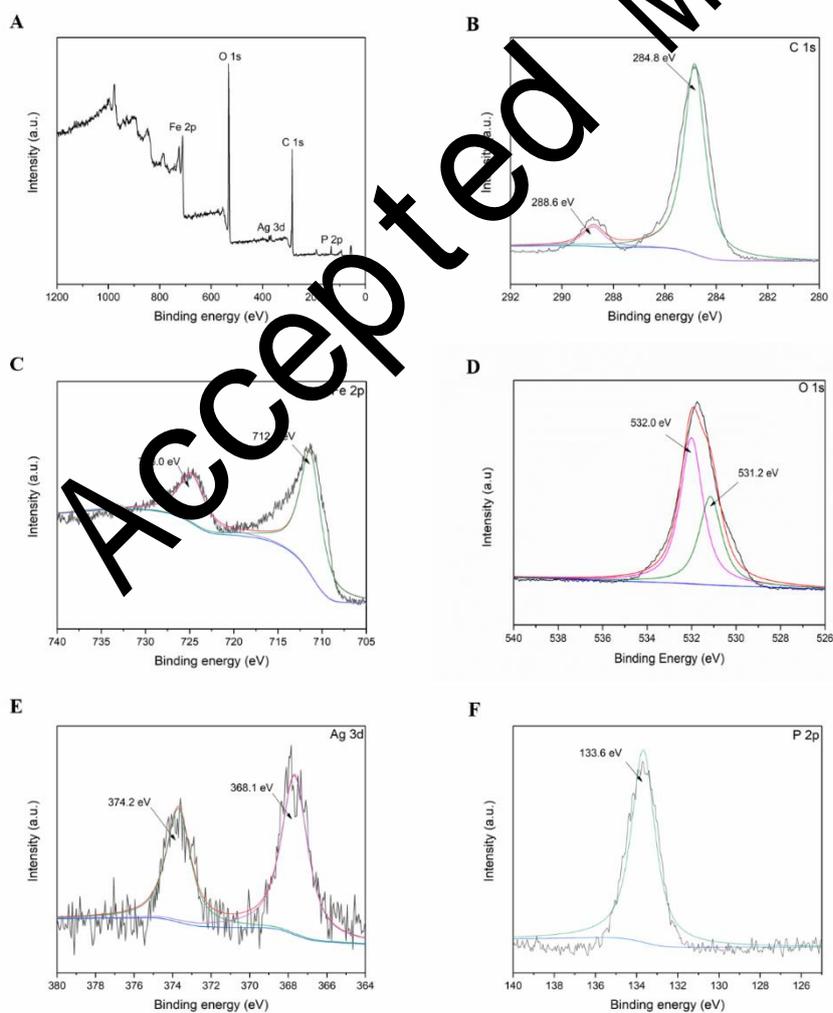
- 462 [70] F. Guo, W. Shi, W. Guan, H. Huang, Y. Liu, Carbon dots/g-C<sub>3</sub>N<sub>4</sub>/ZnO nanocomposite as efficient visible-light  
463 driven photocatalyst for tetracycline total degradation, *Separation and Purification Technology* 173 (2017) 295-303.
- 464 [71] C. Fei, Y. Qi, X. Li, G. Zeng, D. Wang, C. Niu, J. Zhao, H. An, T. Xie, Y. Deng, Hierarchical assembly of graphene-  
465 bridged Ag<sub>3</sub>PO<sub>4</sub>/Ag/BiVO<sub>4</sub> (040) Z-scheme photocatalyst: An efficient, sustainable and heterogeneous catalyst  
466 with enhanced visible-light photoactivity towards tetracycline degradation under visible light irradiation, *Applied*  
467 *Catalysis B Environmental* 200 (2017) 330-342.
- 468 [72] H. Wang, X. Yuan, H. Wang, X. Chen, Z. Wu, L. Jiang, W. Xiong, G. Zeng, Facile synthesis of Sb<sub>2</sub>S<sub>3</sub>/ultrathin  
469 g-C<sub>3</sub>N<sub>4</sub> sheets heterostructures embedded with g-C<sub>3</sub>N<sub>4</sub> quantum dots with enhanced NIR-light photocatalytic  
470 performance, *Applied Catalysis B Environmental* 193 (2016) 36-46.
- 471 [73] C. Liang, C.G. Niu, M. Shen, S.F. Yang, G. Zeng, Controllable fabrication of novel heterojunction composite:  
472 AgBr and Ag@Ag<sub>2</sub>O co-modified Ag<sub>2</sub>CO<sub>3</sub> with excellent photocatalytic performance towards refractory pollutants  
473 degradation, *New Journal of Chemistry*, 2018, 42(5): 3270-3281.
- 474 [74] F.A. Sofi, K. Majid, Enhancement of the photocatalytic performance and thermal stability of an iron based  
475 metal-organic-framework functionalised by Ag/Ag<sub>3</sub>PO<sub>4</sub>, *Materials Chemistry Frontiers* 2(5) (2018) 942-951.
- 476 [75] Y. Han, H. Shi, C. Bai, L. Zhang, J. Wu, H. Meng, Y. Xu, X. Zhang, Ag<sub>3</sub>PO<sub>4</sub>-Mn<sub>2</sub>-53(Fe) Composites with Visible-  
477 Light-Enhanced Photocatalytic Activities for Rhodamine B Degradation, *ChemistrySelect* 3(28) (2018) 8045-8050.
- 478
- 479

Accepted MS



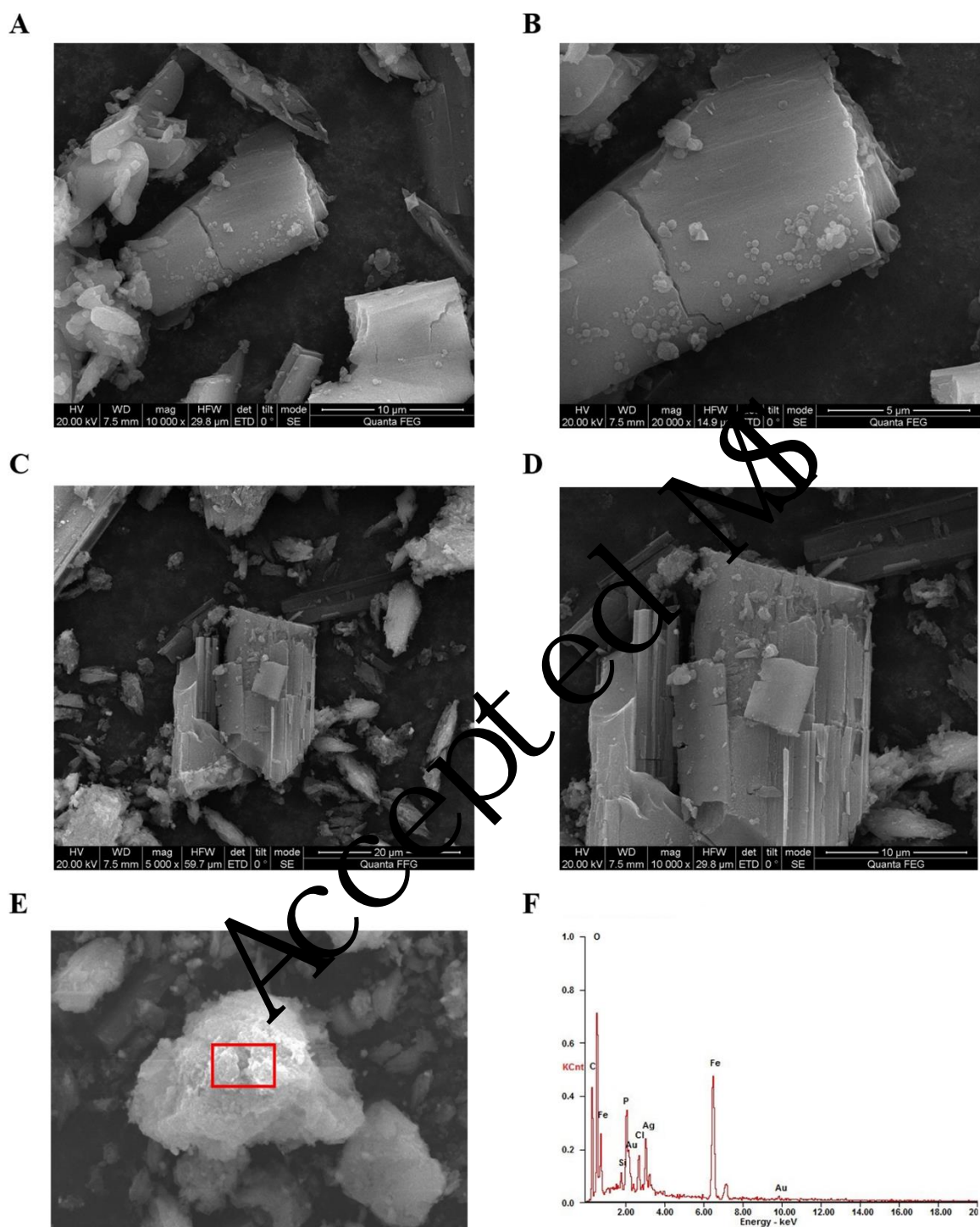
481

482 **Fig 1.** A. XRD patterns of as-prepared samples and B. FT-IR spectra of M:A=10:1, MIL-53(Fe), and  $\text{Ag}_3\text{PO}_4$ .



483

484 **Fig 2.** The XPS spectra of M:A=10:1: A. survey spectra, B. C 1s, C. Fe 2p, D. O 1s, E. Ag 3d, and F. P 2p.



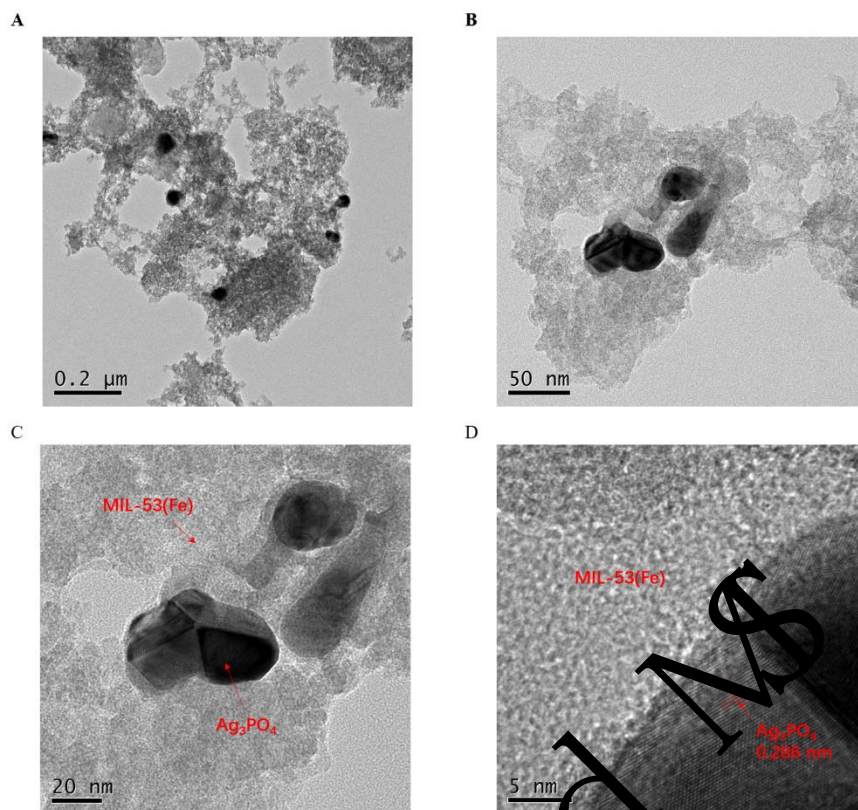
486

487 **Fig 3.** A and B. SEM images of MIL-53(Fe); C, D and E. SEM images of M:A=10:1; F. EDS image of

488

M:A=10:1.

489



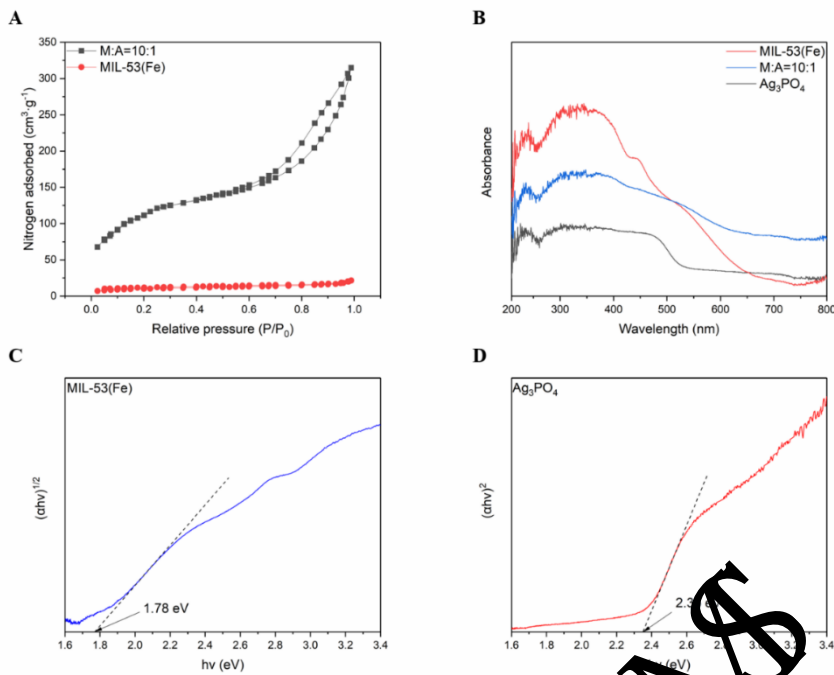
490

491

492

**Fig 4.** TEM images of M:A=10:1.

Accepted MS

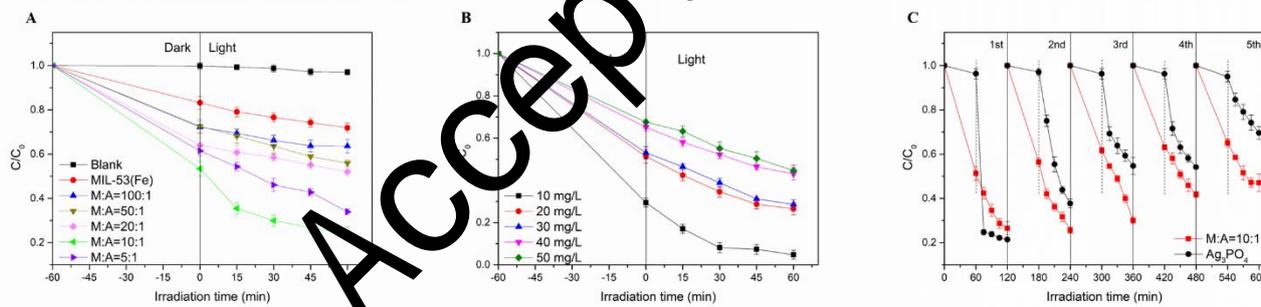


493

494 **Fig 5.** A. Nitrogen adsorption-desorption isotherm of the as-prepared MIL-53(Fe) and M:A=10:1, inset shows

495 the pore size distribution curves; B. UV-vis DRS spectra of MIL-53(Fe), Ag<sub>3</sub>PO<sub>4</sub>, and M:A=10:1 sample; C.

496 band gap energy of MIL-53(Fe), and D. band gap energy of Ag<sub>3</sub>PO<sub>4</sub>.

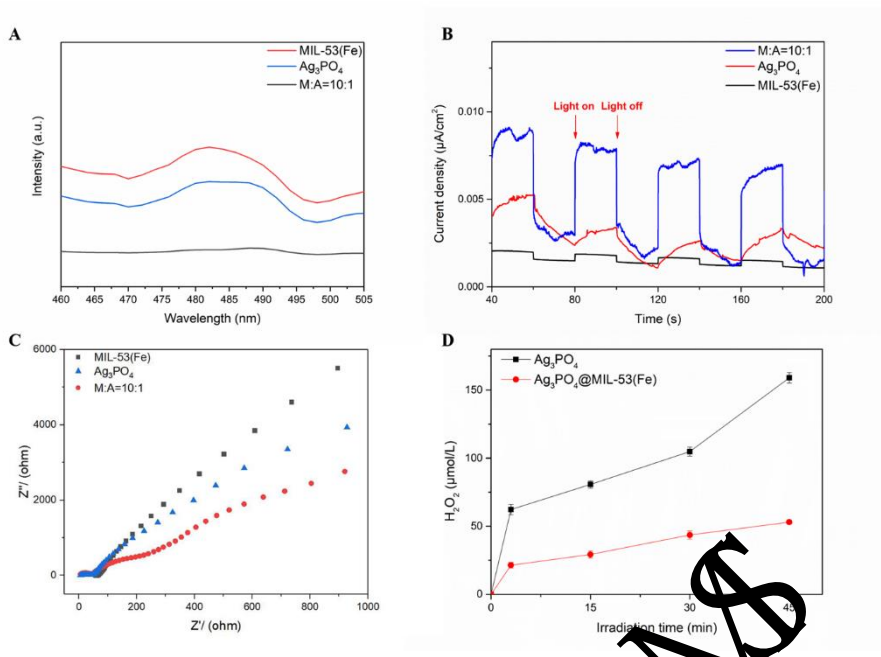


497

498 **Fig 6.** A. photocatalytic degradation of 20 mg/L TC by different samples; B. effects of the initial

499 concentration of TC on the photocatalytic activities of M:A=10:1 sample; C. cycling photocatalytic tests of

500 M:A=10:1 and Ag<sub>3</sub>PO<sub>4</sub> for degradation of 20 mg/L TC.

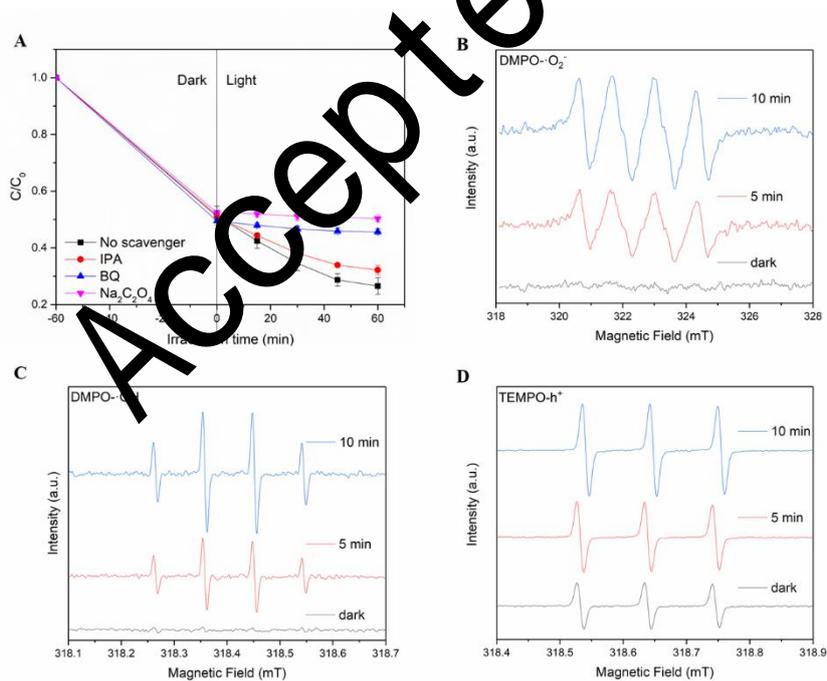


501

502 **Fig 7.** A. PL spectra, B. photocurrent responses, and C. EIS spectra of MIL-53(Fe),  $\text{Ag}_3\text{PO}_4$ , and M:A=10:1;

503

D.  $\text{H}_2\text{O}_2$  concentration detection of M:A=10:1 and  $\text{Ag}_3\text{PO}_4$  under visible light irradiation.



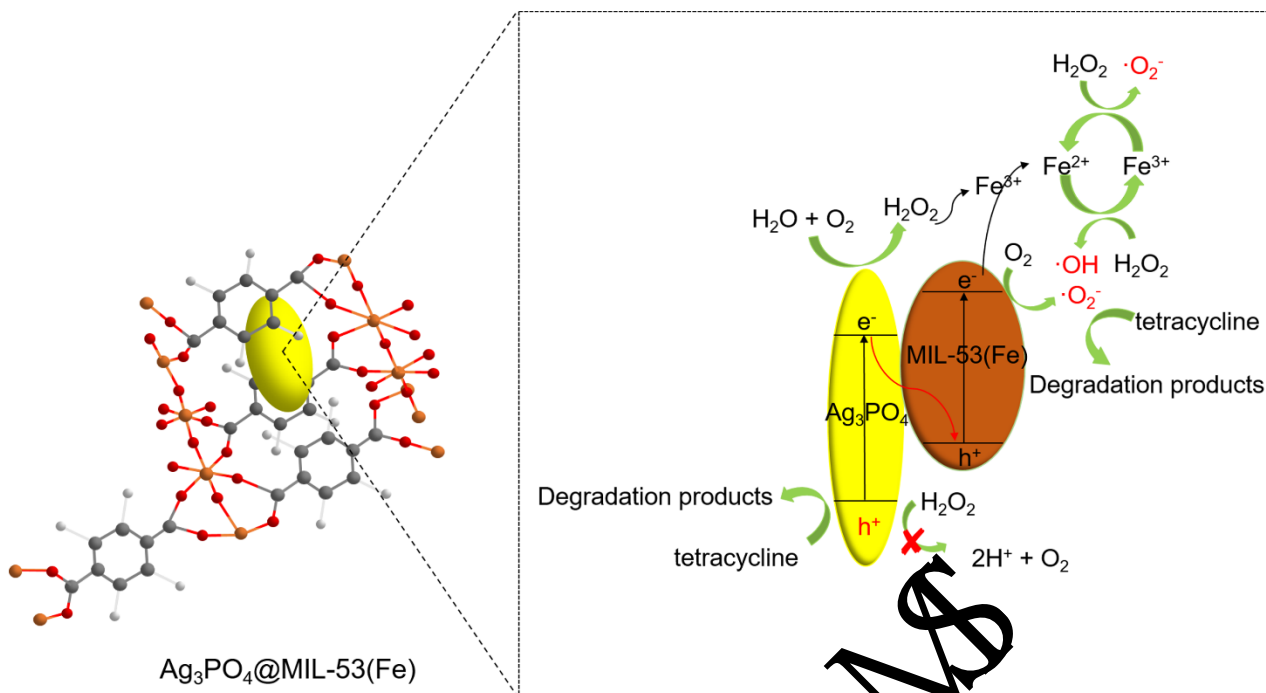
504

505 **Fig 8.** A. photocatalytic curves of M:A=10:1 sample with different scavengers for the degradation of TC; B.

506 Spin-trapping ESR spectra for M:A=10:1 in methanol dispersion for  $\text{DMPO} \cdot \text{O}_2^-$ ; C. in aqueous dispersion for

507

$\text{DMPO} \cdot \text{OH}$ ; and D. in aqueous dispersion for  $\text{TEMPO} \cdot \text{h}^+$  under both dark and visible light irradiation.



508

509 **Fig 9.** Proposed photocatalytic mechanism in  $\text{Ag}_3\text{PO}_4@\text{MIL-53}(\text{Fe})$  yolk-shell structure composites.

510 **Table**

511 **Table 1.** Surface area, pore size, and pore volume data for MIL-53(Fe) and M:A=10:1

Samples	Surface area ( $\text{m}^2/\text{g}$ )	Pore size (nm)	$V_t$ ( $\text{cm}^3/\text{g}$ )
MIL-53(Fe)	3.866	3.919	0.024
M:A=10:1	37.945	4.896	0.341

512 Note: the pore size distribution of samples were calculated by Barrett-Joyner-Halenda method; and  $V_t$  (total

513 pore volume) were determined at  $P/P_0=0.99$ .

514

515

516